Progress In Electromagnetics Research, Vol. 140, 523–544, 2013

ELECTROMAGNETIC DESIGN AND FEM ANALYSIS OF A NOVEL DUAL-AIR-GAP RELUCTANCE MACHINE

Chockalingam Aravind Vaithilingam[3, *], Norhisam Misron[1, 2], Ishak Aris[1], Mohammad Hamiruce Marhaban[1], and Masami Nirei[4]

[1]Department of Electrical and Electronics, University Putra Malaysia, Selangor, Malaysia

[2]Institute of Advanced Technology (ITMA), Universiti Putra Malaysia, Serdang, Selangor 43400, Malaysia

[3]School of Engineering, Taylor's University, Selangor, Malaysia

[4]Nagona College of Technology, Japan

Abstract—The electro-magnetic torque production in the reluctance machine is highly influenced by the magnetic linkages in the air-gap area. The conventional machines derive the drawback of reduction in the air-gap area to a minimal due to influence of mechanical unbalancing thereby restricting the effective energy conversion area. In order to increase the magnetic linkage area, the dual-air-gap structure is introduced. The dual-air-gap structure is realised through the division of the magnetic circuit area into two air-gaps while still maintaining the net air-gap length value. A double-rotor with single-stator structure is used to attribute the above concept. The electro-magnetic analysis of such a structure is developed and investigated through numerical analysis. In order to validate the proposed structure the electro-magnetic characteristics are compared with that of the conventional structure at similar operating conditions. The maximum torque generated by the selected dual-air-gap structure is 1.7549 Nm and for conventional structure is 1.2723 Nm. The evaluation of the proposed machine is done at the same operating conditions and it is found that the dual-air-gap structure exhibit 65% increase in average torque value in comparison with that of the conventional single-air-gap structure.

Received 20 February 2013, Accepted 31 May 2013, Scheduled 19 June 2013

* Corresponding author: Chockalingam Aravind Vaithilingam (aravindcv@ieee.org).

1. INTRODUCTION

With its simple structure, absence of winding in rotor side, fault tolerant capability, low cost with no permanent magnet either in the stator or in the rotor, reluctance machine is a better choice of motor under adverse conditions [1]. The torque production in reluctance motor is derived from the tendency of the non-magnetic rotor poles tending to align with that of the nearest excited stator poles [2]. With the corresponding stator coil excitations, the rotor experiences a force that pulls the rotor from the full non-overlap position to the full overlap position. The traverse of this pull is influenced by the swept angle (called as pole-arc) between the poles. The flux linkage area determines the permeance (inverse of reluctance) in the magnetic circuit and thereby the torque producing capability. In order to increase the flux linkage area, a dual-air-gap structure is proposed through the double-rotor structure [3]. The early concepts of introduction of double-stator or rotor structure are finding new dimensions in developing high power density machines. The double-stator structure is extensively progressive in applications related to the development of the permanent magnet brush-less machines [4–6]. The application of the use of double-stator for wind energy application is presented in [7]. Two stators for the bearing-less reluctance type of machine are put forward in [8]. The double-stator structure increases the coil spacing however it increases the volume and also increases the losses inside the machine. On the contrary to the double-stator structure, the double-rotor structure is researched mostly based on the application requirements. Double-rotor motor feasibility is proposed in [9] as applied to the deployment in hybrid electric vehicle. In electric vehicle development where the two wheels are need to be connected for differential action is proposed in [10]. The electro-magnetic design and analysis of double-rotor flux modulated permanent magnet machines is put forward in [11]. The dual-layer rotor reluctance generator is presented in [12] using finite element analysis. The double-rotor structure with independent operation of the two rotors using simulation is presented in [13]. In this research the double-rotor single-stator structure to realise the dual-air-gap, as confined with the name as Double Rotor Reluctance Motor (DRRM) is investigated. Section 2 presents the features of the inductance profile of the machine and its influence in the torque generation. Section 3 presents the design aspects in the dual-air-gap structure used in this design. Section 4 presents the electromagnetic analysis through finite element tool. Section 5 presents a comparative evaluations of the proposed structure with that of the conventional structure.

2. INDUCTANCE PROFILE

Figure 1 shows the rotor moving for one pole pitch from the full non-overlap position to full overlap position and back to full non-overlap position for a typical reluctance machine. β_s and β_r represent excited stator pole and rotor pole-arc, respectively. As can be seen at both the extreme positions (at full overlap and full non-overlap positions), no useful energy is converted rather is stored inside the machine as field energy. The useful output torque is developed only as the rotor roll over the stator. As the machine is moving from the full non-overlap position to the full overlap position, the motoring torque (Figure 1(a)–Figure 1(e)) is developed, and during the energy released as the rotor is moving away from the full overlap position to the full non-overlap positions the generating torque (Figure 1(e)–Figure 1(i)) is developed. Table 1 shows the properties at the extreme positions of the rotor

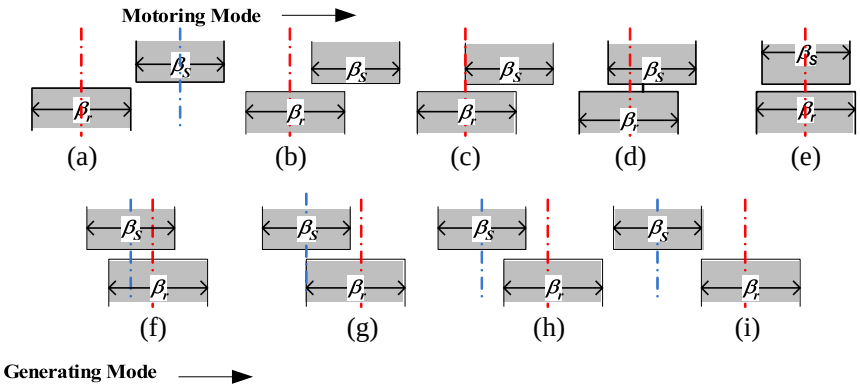

Figure 1. Motoring and generating mode. (a) Full non-overlap, (b) 1/4th of poles interact, (c) 1/2th of poles interact, (d) 3/4th of poles interact, (e) full overlap, (f) 3/4th of poles interact, (g) 1/2th of poles interact, (h) 1/4th of poles interact, (i) full non-overlap.

Table 1. Properties of full non-overlap and full overlap position.

Property	Full Non-overlap	Full Overlap
Position angle	$\pm 90°$	$0, 180°$
Inductance value	Minimum	Maximum
Saturation	unlikely	most likely
Torque	zero	zero
Equilibrium	unstable	stable

movement. As can be seen, during the full non-overlap position, the machine is stable; however the core tends to saturate rapidly during the full overlap position, the equilibrium is not realized. The range of operation of the two extreme positions influence the torque generating capability to a larger extent and hence it is expected the rotor to spend less time in both the extreme positions. As the rotor traverses (depends on the pole arc values of the stator and the rotor) between the extreme positions, the flux linkage area is increased and thereby improving the torque generating capability.

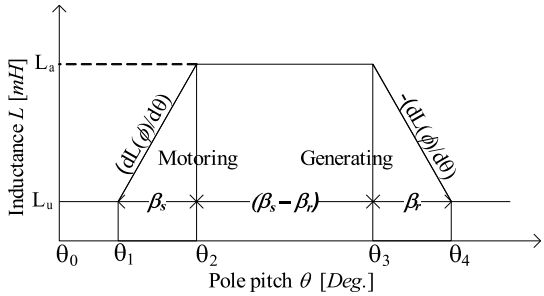

Figure 2. Inductance profile.

Figure 2 represents the ideal inductance characteristics for motoring conditions (θ_1 and θ_2) and for the generating conditions (θ_3 and θ_4). For the motoring conditions, the torque equation is as in Equation (1).

$$T_e = \left(\frac{1}{2}\right)(i^2)\left[\frac{L_a - L_u}{\beta_s}\right] \tag{1}$$

where L_a is the completely overlap inductance and L_u the completely non-overlap positions. The instantaneous torque developed can be written as in Equation (2).

$$T_e = \left[\frac{(i)^2}{2\beta_s}\right]\left[\frac{dL(\phi)}{d\theta}\right] \tag{2}$$

But the inductance L is proportional to the permeance P at the point of contact and given as in Equation (3).

$$L = N^2 P \tag{3}$$

where N is the number of turns. Hence the above equation can be written as in Equation (4).

$$T_e = \left[\frac{(i \cdot N)^2}{2\beta_s}\right]\left[\frac{dP(\phi)}{d\theta}\right] \tag{4}$$

The permeance variation term introduces the structural characteristics that depends on the flux linkage contact area as in Equation (5).

$$P = \frac{\mu_{\circ} A_g}{l_g} \tag{5}$$

where A_g defines the swept pole face area (pole-arcs), and l_g represents the radial length of the air-gap. This pole swept area depends on the pole-arc of the stator and the rotor that is involved during the energy conversion cycle of the machine. For the impressed current, the magnetic flux is the product of the magnetic flux density B_g and air-gap area A_g. Therefore, the electromagnetic torque is given as in Equation (6).

$$T_e = \left[\frac{(B_g A_g N)^2}{2\beta_s}\right]\left[\frac{dP(\phi)}{d\theta}\right] \tag{6}$$

In generic form the swept area during the motoring condition is given as in Equation (7).

$$A_g = (\beta_s)(D_s)L_{stk} \tag{7}$$

where L_{stk} is the stack length, D_s the diameter of the stator, with the assumption that the stator pole-arc value is greater than the rotor pole-arc value.

3. CONCEPT OF DUAL-AIR-GAP STRUCTURE

3.1. Design Concepts

Figure 3 shows the magnetic circuit for the long flux flow in the conventional reluctance machines. As can be seen with the excited stator pole the flux traverses through the upper air-gap (l_{g1}) and

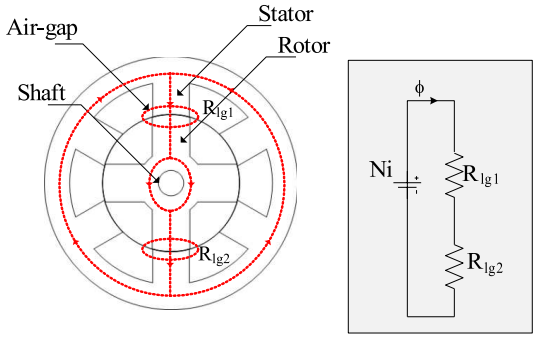

Figure 3. Conventional reluctance machine magnetic circuit.

through the lower air-gap (l_{g2}) to complete the magnetic circuit. The air-gap length in the conventional reluctance motor is restricted to a minimal value as it introduces mechanical imbalance during operation. This affects the torque producing capability of the machine. Secondly, the area of flux linkages as the rotor moves over the stator is influenced by the extent of pole-arc as the flux traverse in the air-gap. The extension of the division in the air-gap length is derived with the introduction of the dual-air-gap with still maintaining the net air-gap length thereby maximising the air-gap surface area. This dual-air-gap necessitates the modification in the machine structure either through double rotors with single stator or through double stators with single rotor. In brush-less DC machines, it is a common trend to use configurations of double stators for maximising the net magneto-motive force. However, the double-stator structure leads to the increase in the number of turns and hence the loss inside the machine. The reluctance value at the air-gap is given as in Equations (8), (9).

$$R_{lg1} = \frac{l_{g1}}{\mu_0(\beta_s)(D_s)(L_{stk})} \tag{8}$$

$$R_{lg2} = \frac{l_{g2}}{\mu_0(\beta_s)(D_s)(L_{stk})} \tag{9}$$

Therefore, the net reluctance R_{lg} value in the air-gap is given as in Equation (10).

$$R_{lg} = \frac{2l_g}{\mu_0(\beta_s)(D_s)(L_{stk})} \tag{10}$$

where

$$l_g = l_{g1} + l_{g2}; \quad R_{lg} = R_{lg1} + R_{lg2} \tag{11}$$

Therefore, the flux linked is given by Equation (12).

$$\phi = \frac{(Ni)\mu_0(\beta_s)(D_s)(L_{stk})}{2l_g} \tag{12}$$

Figure 4 shows the magnetic circuit for a typical double-rotor structure and the magnetic circuit (the net air-gap length is still maintained). As can be seen, the air-gap length is divided, and hence the reluctance at each of the air-gap is reduced by half as in the Equations (13), (14).

$$R_{lg1} = \frac{l_{g1}}{2\mu_0(\beta_{os})(D_{os})L_{stk}} \tag{13}$$

$$R_{lg2} = \frac{l_{g2}}{2\mu_0(\beta_{is})(D_{is})L_{stk}} \tag{14}$$

The reluctance value is given as

$$R_{lg} = 2(R_{lg1} + R_{lg2}) \tag{15}$$

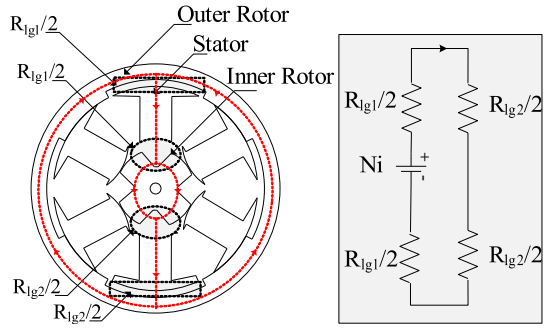

Figure 4. Proposed double-rotor reluctance machine magnetic circuit.

Therefore, the flux linked is given as in Equation (16)

$$\phi = (NiL_{stk}\mu_0)\frac{\beta_{os}\beta_{is}D_{is}D_{os}}{l_{g1}\beta_{is}D_{is} + l_{g2}\beta_{os}D_{os}} \tag{16}$$

The length of the air-gap needs to be kept at the same value for symmetric rotation about the center $l_{g1} = l_{g2}$, then the flux linked is given as in Equation (17).

$$\phi = \frac{NiL_{stk}\mu_0}{l_g}\frac{\beta_{os}\beta_{is}D_{is}D_{os}}{\beta_{is}D_{is} + \beta_{os}D_{os}} \tag{17}$$

The flux linkage depends on the pole arc interactions values as the physical dimension is fixed for the machine. This analysis is done based on the assumption that the stator pole-arc is bigger than the rotor to establish the relation of the flux linked to that of the pole-arc. However, this analysis can be extended for the case of the rotor pole-arc bigger than the stator pole-arc, in which case the self-starting capability at any point is difficult.

3.2. Limitations on Pole-arc Values

The design considered in this analysis is of 6 stator poles and 4 rotor poles, typically referred as a 6/4 machine. However, the concept can be extended to any applicable possible combinations [2]. For the 6 stator pole machine the stator pole pitch is 60°. For self starting condition of the motor the minimum swept angle ($\beta_{\min}$) is given by

$$\beta_{\min} = \frac{4\pi}{N_s N_r} \tag{18}$$

where N_s and N_r are the numbers of stator and rotor poles respectively. To make the machine as self starting the minimum pole-arc value is to be 30°. With the given considerations for a pole enclosure clearance in between the adjacent stator poles as 5°, the available range of the

pole-arc variations is between 30° to 50°. Figure 5 shows the pole arc limitations on the machine pole. As seen, the maximum rotor pole pitch is (β_{sm}) which is 60°, and to give a clearance on the both sides a clearance angle of $\beta_{sc} = 5°$ is provided. With considerations for the pole enclosure clearance in between the adjacent stator poles as 5 deg, the possible range of the pole arc is between 30° and 50°. On the rotor pole-arc possible values, once again the minimum pole-arc required for sustaining running of the motor needs to be more that 30° (stroke angle). With 4 poles on the rotor, the rotor pole pitch is 90°. With the stator pole pitch at 60° and rotor pole pitch at 90°, the effective traverse angle is 30° (which is the minimum angle required in the movement on the rotor body). Hence the range of rotor pole-arc is between 30° and 60° to maintain the traverse angle. Once again to pertain to the pole enclosure, a clearance of 5° is given on both sides of the symmetrical pole, and hence the range is between 30°–50°.

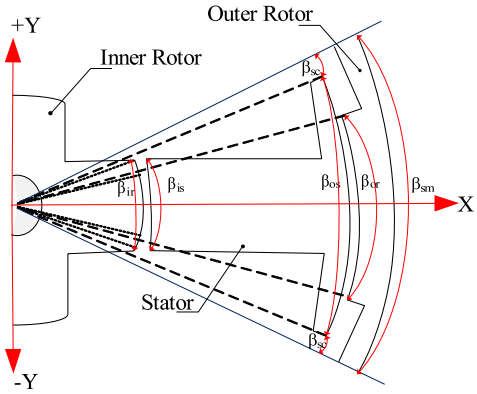

Figure 5. Pole-arc limitations.

The limit on the overlap angle for self-starting is given as in Equation (19), which is 15°.

$$\max[\theta_\circ] = \frac{2\pi}{N_r}\left(\frac{1}{2} - \frac{1}{q}\right) \tag{19}$$

where q is the number of phases. The limit or the possible range for the rotor pole is between 30° and 45°. With four feasible pole-arc possibilities and with a 5° possible interval in the pole angle, the possible combination is r^n where r is the possible pole angle interval and n the pole arc parameter. In this case, the possible n value is between 0 and 5, and r for a chosen interval of 5°. With the constraints of both the stator and rotor pole arcs being the same value and with a

minimum clearance of 15°, the possible differences in pole-arcs are 0°, 5°, 10°, 15°. Using FEA tool with the constraints as in Table 2, the possible best combinations are derived [14].

Table 2. Design consideration constraints.

Constraints	Condition
Rotor Pole Pitch (θ_r)	$\frac{2\pi}{N_r}$
Stator Pole Pitch (θ_s)	$\frac{2\pi}{N_s}$
Phase Displacement Angle	$\frac{\theta_r}{\frac{N_s}{2}}$
Self-starting (min[β_s])	$\frac{4\pi}{N_s N_r}$
Motoring Slope Range (β_s)	$\frac{dL}{d\theta}$
Minimum Overlap Angle Min (θ_0)	dead-zone
Minimum Overlap Inductance Value	$\frac{1}{2}\left[\frac{2\pi}{N_r} - (\beta_{os} + \beta_{or})\right]$
Minimum Overlap Inductance Value	$\frac{1}{2}\left[\frac{2\pi}{N_r} - (\beta_{is} + \beta_{ir})\right]$
Maximum Overlap Angle Max (θ_0)	$\frac{2\pi}{N_r}(\frac{1}{2} - \frac{1}{q})$
Maximum Overlap Inductance Value	$\left(\frac{\beta_{os}}{2} - \frac{\beta_{or}}{2} + \frac{\pi}{N_r}\right)$
Maximum Overlap Inductance Value	$\left(\frac{\beta_{is}}{2} - \frac{\beta_{ir}}{2} + \frac{\pi}{N_r}\right)$

4. FINITE ELEMENT ANALYSIS

Finite Element Analysis (FEA) is used to compute the magnetic characteristics, but this necessitates a package and more time for modelling the motor and is used extensively by researchers in machine design. Most of them use computational tools to demonstrate the first hand information on the property of the machine [15–17]. The FEA tool used in this investigation is developed based on the nodal force method [18]. This method is similar to the method of finding equivalent nodal force from distributed load force in stress analysis. The magnetic volume and surface forces are through the Maxwell stress tensor using the Eistein's summation convention. For any three-dimensional volume of boundary surface $\mho$, T_{ik} is the stress tensor and n the unit vector from region 1 to region 2 perpendicular to the surface then the Maxwell

stress tensor is given by Equation (20).

$$T_{ik} = (H_i)(B_k) - (\delta_{ik})\rho^{co} \tag{20}$$

where δ is the Kroneckers delta (here ρ^{co} is a piecewise function of variables i and k with the value being 1 when $i = k$ else it is zero) and the co-energy density given in Equation (21).

$$\rho^{co} = \int_0^H BdH \tag{21}$$

In FEM calculation that uses the Maxwell method alone, the discontinuity occurs due to the interpolation functions at the element interfaces. The nodal force f_{ni} is then given as in Equation (22).

$$f_{ni} = \left(- \int T_{ik}\delta_k w_n \right) d\mho \tag{22}$$

In the above Equation (22), the integration is over the elements that connect the nodes in the design. The virtual displacement for the work done by the magnetic force is given as in Equation (23).

$$\delta W = \sum_n \left(- \int T_{ik}\delta_k w_n d\mho \right) \delta u_{ni} \tag{23}$$

where w_n is the nodal shape function and δu_{ni} the virtual nodal displacement. With no spatial differentiation of the field quantities of B, H is needed, and the discontinuity of the calculated field causes no difficulties. The resultant force is calculated by summation of the nodal forces at various nodes in the body. The formulation does not depend on the interpolation functions as used in other FEA tools. Hence the results originated from this FEA tool are highly accurate even though the computation calculation is heavier. In order to make the FEM calculations more accurate, there are six circular tubes that are constructed in the programming design in the two-air-gap surface as in Figure 6. The design sequence in the programming of the FEA in this investigation is as in Figure 7. It involves three stages. The first one is the development of model based on the design parameters, the setting of the mesh points and the configuration settings including the number of turns, the impressed current. The second stage is the computations of the designed model. The third stage is to derive the magnetic and mechanical values from the computations results. The extraction of the data is through the mathematical tool (Microsoft excel), and the analysis for the machine performance can be done through analytical tool (Origin mathematical tool). The automatic variations on the parameter can be set in the analysis, and hence the

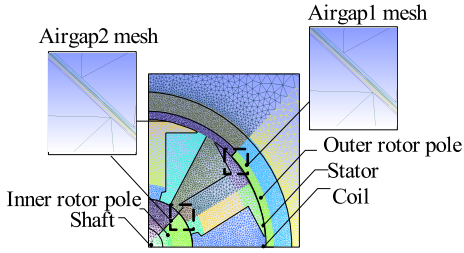

Figure 6. Air-gap layers.

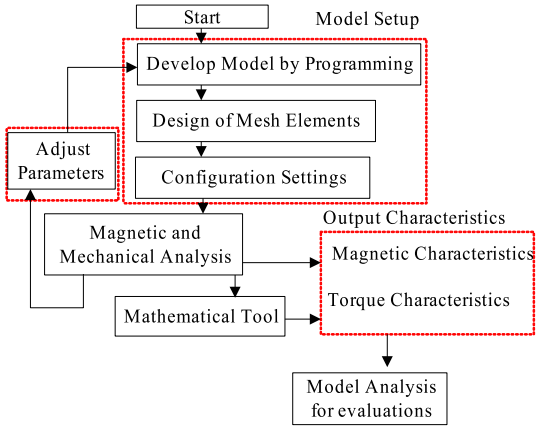

Figure 7. FEA analysis procedure.

computation is relatively easier once the basic mechanical structure is constructed using the FEA programming tool.

The computation of one value over a rotor pole pitch with 1 degree interval took about 2 minutes 35 seconds. From the FEA analysis, the best possible combinations of pole arcs are $\beta_{os} = 50°$, $\beta_{is} = 30°$, $\beta_{or} = 35°$ and $\beta_{ir} = 45°$. The selection of this structure is based on the model that gives better average torque with less harmonics. A detailed analysis is presented in [19]. Figure 8 shows the final structure in the design, and Table 3 shows the dimensions of the proposed structure.

4.1. Magnetic Characteristics

Figure 9(i) shows the completely non-overlap flux flow, and as can be seen, the flux flow is uniform in both sides of the machine. In other words, it is a stable state with no torque generated. However, variation in the pole-arc values is influenced by the change in the flux pattern and thereby the inductance and torque of the machine, which can be observed during the partial overlap positions. Figures 9(ii)–9(v) show

Table 3. Double-rotor reluctance motor specifications.

Parameter	Symbol	Value
Outer Diameter	D_o	80 mm
Outer rotor diameter	D_{or}	66.6 mm
Dual-Air-gap (each)	l_g	0.05
Inner rotor diameter	D_{ir}	51.9 mm
Shaft Diameter	D_{sh}	14 mm
Stack Length	L_{stk}	40 mm
Turns per phase	N	80 mm
Rated Current	i	6.12 A
Outer Rotor Pole Arc	β_{or}	35 deg
Inner Rotor Pole Arc	β_{ir}	45 deg
Outer Stator Surface Pole Arc	β_{os}	50 deg
Inner Stator Surface Pole Arc	β_{is}	30 deg

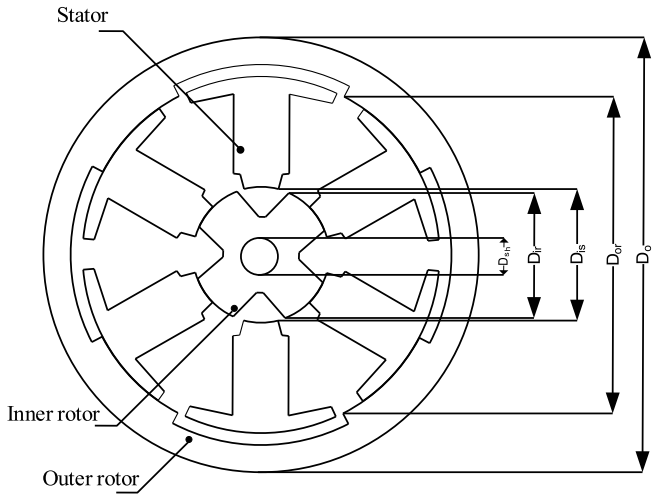

Figure 8. Final structure of DRRM.

the partial overlap at a case when the rotor pole is in motion. The flux flow can be considered as three different regions of flow. The flux flow in the middle is uniform, and the flux flow entering the upper part leaves the lower part and vice versa. This can be observed in the other partial overlap position shown in Figure 9(iii) wherein ($\frac{1}{4}$)th stator and rotor are facing each other. Figure 9(vi) shows the flux flow under the

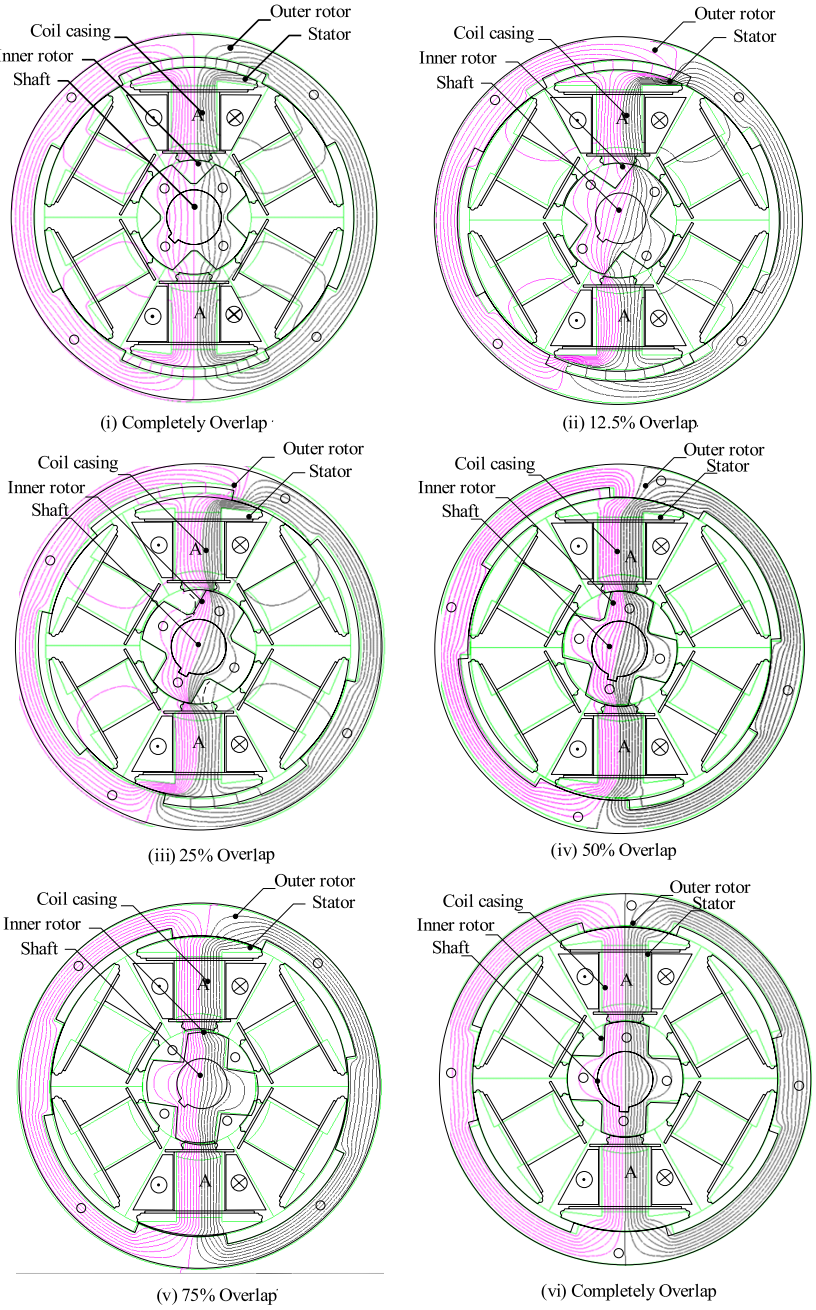

Figure 9. Flux flow at various rotor position.

full overlap positions. Similar to the case of non-overlap position, the useful torque generation is null. However, a smaller angle displacement influences the flux flow, and thereby the torque value starts to build-up. With the unsymmetrical design values extended inductance profile (which is a function of the flux linkage for the injected current) is derived. The extended inductance slope increases the co-energy surface area (W_{co}) over the same rotor pole pitch thereby increases the torque to a higher value.

Figure 10 shows the co-energy area derived for the DRRM. The co-energy value is derived from the integration of the area shown in the bounded region. As the torque generated is proportional to the energy variation of operation this characteristic provides knowledge on the machine characteristics. The co-energy value for the DRRM is computed using Equation (24).

$$T_e = \frac{\delta W_{co}}{\delta \theta} = \frac{1}{2}\left[\frac{L_a - L_u}{\theta_a - \theta_u}\right] i^2 \tag{24}$$

Figure 11 shows the inductance characteristics of the DRRM with different current value. As can be seen, inductance varies as the current injected is increased. However, the increase of current is accompanied by the heating loss in the coil. Since the machine is sequentially excited and not continuously excited, the heat loss is considerably smaller than its counter-part machines [1]. The functionality operation of such a type of machine with the driver circuit is available in [20]. The cut-way representation of the fabricated DRRM is as shown in Figure 12.

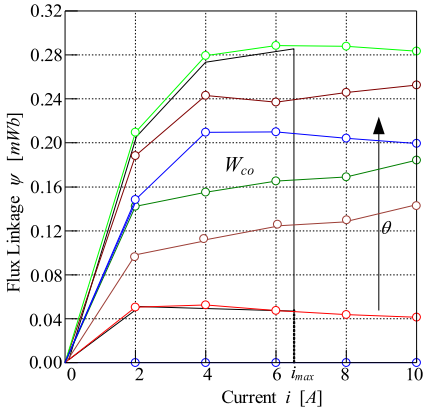

Figure 10. Flux linkage characteristics.

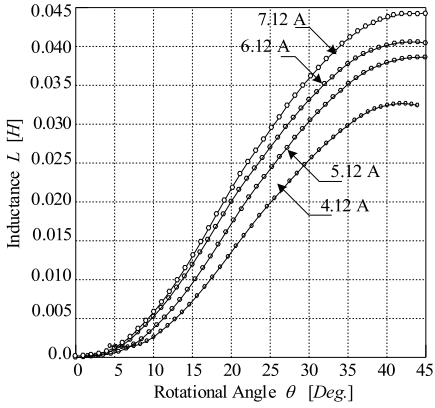

Figure 11. Inductance characteristics with different current excitation.

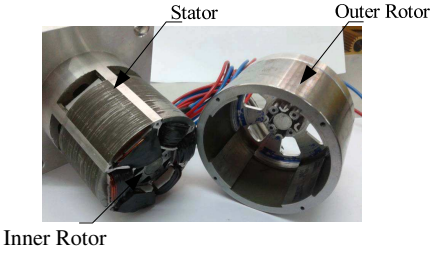

Figure 12. DRRM cutway view.

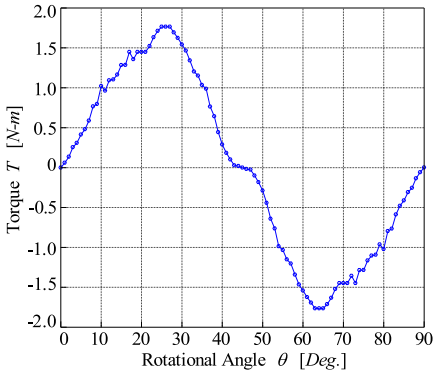

Figure 13. Static torque characteristics.

4.2. Static Torque Characteristics

Figure 13 shows the static numerical characteristics of the DRRM. As can be seen, the torque characteristics is closer to sinusoidal, and hence the Total Harmonic Distortion (THD) is lower. The maximum torque achieved is about 1.7549 N.m with the average torque value of 0.953 N-m with a THD of 13.4% through the FEA analysis. Figure 14 shows the torque characteristics with various mmf values. It is imperative that with higher mmf value the torque generated is higher, but it comes with the compromise on the increase of size to accommodate for the increase in the number of turns or bigger conductor size. This increases the copper losses inside the machine. The mmf for the designed machine is kept at 673.2 AT. Figure 15 shows the three-phase sequential excitation of the DRRM through FEA. The torque ripple between the phases is found to be about 10.55%.

5. COMPARISON OF CRM AND DRRM

5.1. Parametric Design

To perform a comparative evaluations of the DRRM and the conventional CRM structure, both are built to the same size, volume and similar operating conditions through the FEA tool. Figure 16 shows the concept machine dimensions of the conventional CRM and DRRM. The choice of pole-arc for the CRM is based on [2] and the choice of the DRRM based on the selected value in this design. Both machines are of 6/4 configuration and three phase machine with uniform bore and stack values. Both the machines are constructed and

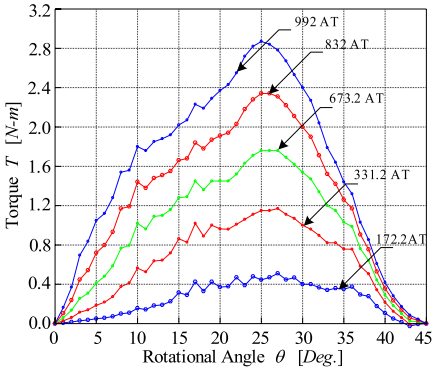

Figure 14. Torque characteristics with different current excitations.

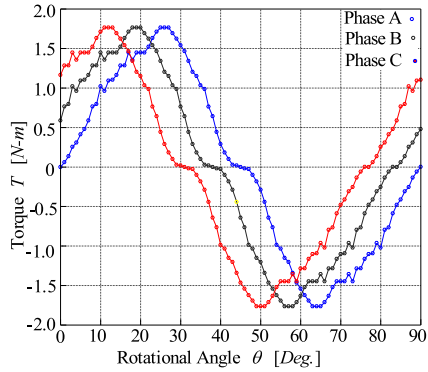

Figure 15. FEA three phase torque characteristics.

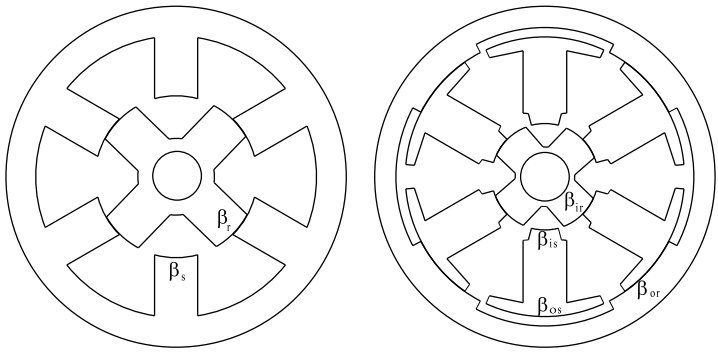

Figure 16. CRM and DRRM configurations.

designed using the same FEA tool for performance evaluations. Table 4 shows the mechanical dimensions of the CRM and DRRM. Both the machines are designed with the same bore length, stack length, and overall mass. As can be seen from the values, the net volume is the same for both the CRM and DRRM; however, the rotor area surface is significantly higher for DRRM as it encloses two rotors.

5.2. Evaluations Parameters

5.2.1. Total Harmonic Distortion

The symmetrical nature of torque profile inside the machine derives reduced or zero ripples in the machine. A quantifiable measure, the total harmonic distortion (THD), which is a measure of the distortion in the signal due to oscillations at the harmonics of the input signal, is

Table 4. Parameter values of CRM and DRRM.

Parameter	**CRM**	**DRRM**
Number of Stator Poles	6	6
Number of Rotor Poles	4	4
Outer Radius of Stator	40 mm	40 mm
Inner Radius of Stator	19 mm	35 mm
Outer Radius of Rotor	18.9 mm	34.95 mm
Inner radius of rotor	8 mm	13 mm
Stack Length	40 mm	40 mm
Stator Pole-arc (β_s)	35°	–
Stator Inner Teeth Pole-arc (β_{is})	–	30°
Stator Outer Teeth Pole-arc (β_{os})	–	50°
Rotor Pole-arc (β_r)	30°	–
Outer Rotor Pole-arc (β_{or})	–	45°
Inner Rotor Pole-arc (β_{ir})	–	35°
Number of Phases	3	3
Air gap Length (lg)	0.1 mm	–
Outer Air-gap Length ($lg1$)	–	0.05 mm
Inner Air-gap Length ($lg2$)	–	0.05 mm
mmf	673.2 AT	673.2 AT
Stator Area	30158.93 mm^2	25137.88 mm^2
Stator Mass	98.57 gms	58.79 gms
Rotor Volume	25625.58 mm^3	66574.74 mm^3
Rotor Area	7799.19 mm^2	27185.97 mm^2
Rotor Mass	25.63 gms	66.57 gms
Net Volume	124198 mm^3	125367 mm^3

used as a factor to evaluate the ripple and is defined as in Equation (25).

$$\text{THD} = \frac{\sqrt{\sum_{i=2}^{\infty}(F_i)^2}}{F_1} \tag{25}$$

5.2.2. Motor Constant Square Density

The motor constant square density (G) is a motor performance parameter of the motor to transform electrical power to mechanical

power and is a valuable tool for the application engineer particularly for recommending a best fit replacement for a competitors motor [6]. This constant is chosen since it relates to the torque, power and volume of the motor. The motor constant square density is given as in Equation (26).

$$G = \frac{(k_m)^2}{V} \tag{26}$$

where V is the volume of the motor and the motor constant k_m is given as in Equation (27).

$$k_m = \frac{k_t}{\sqrt{P_{in}}} \tag{27}$$

and the torque constant k_T is stated as in Equation (28).

$$k_t = \frac{T_f}{I} \tag{28}$$

5.3. Comparative Evaluations

5.3.1. Magnetic and Mechanical Characteristics

Figure 17 shows the static torque characteristics of the CRM and the DRRM. Figure 18 shows the motoring slope characteristics of both the CRM and DRRM. As can be seen, compared to the DRRM, although the slope value of the CRM is higher, the motoring characteristic reaches the constant value at about 15°. In other words, it reaches the dead-zone where the slope is constant, hence the torque generating capability is reduced. However, the slope value for the DRRM is

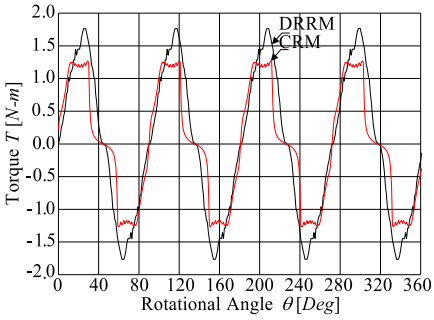

Figure 17. Comparison of the torque characteristics.

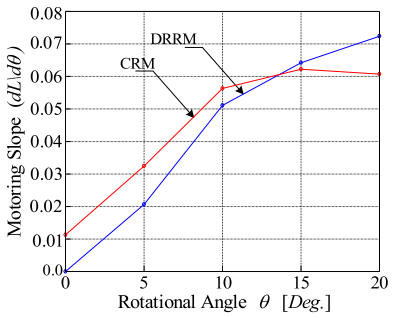

Figure 18. Comparison of the motoring slope characteristics.

linear and extend till 20° which shows the extended torque generating capability. Hence the torque value is better than that of the CRM.

Figure 19 shows the torque characteristics with different mmf values. As the torque generation is a function of impressed current, it is worth of this analysis. In the conventional machine for lower mmf value, the torque characteristics are relatively uneven, whereas for the proposed DRRM the torque pattern at various mmf values is almost symmetrical.

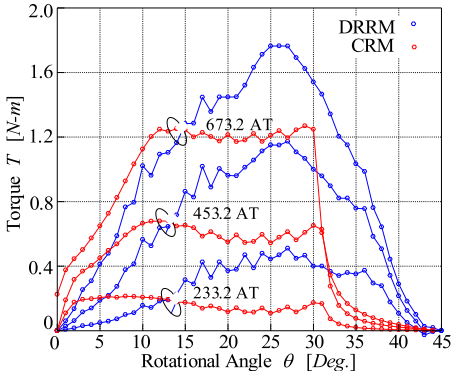

Figure 19. Comparison of torque characteristics with different mmf values.

5.3.2. Loss Characteristics

The core-loss is computed based on Figure 20. With the flux density value, the iron loss of the system is computed. The total loss of the machine at any one rotor position is computed by multiplying the weighing factor and operating frequency. The loss characteristics computed through analytical and simulation for both the motors aew as shown in Figure 21.

5.3.3. Quality Factor

Figure 22 shows the THD comparisons of the two models. It is inferred that the DRRM increases average torque by 23% with the THD reduced by 79% compared to that of CRM. An improved sinusoidal symmetric waveform is expected to have reduced THD as evident from the analysis. The maximum torque generated by the DRRM is about 1.7549 Nm with the THD value of 13.4%. The maximum torque generated by the CRM is about 1.2723 N-m with THD value of 67.1%. Table 5 shows the comparison of the CRM with DRRM in terms of quality factors.

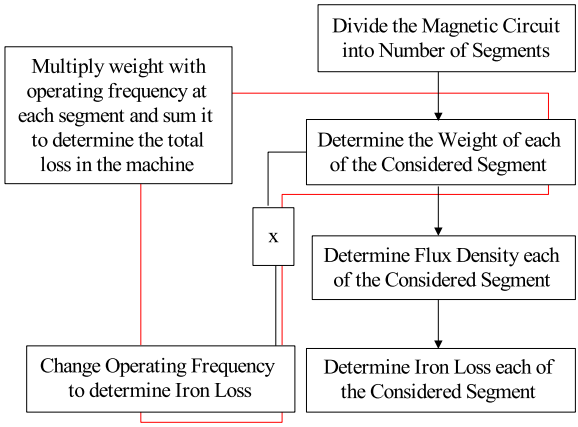

Figure 20. Core-loss computation method.

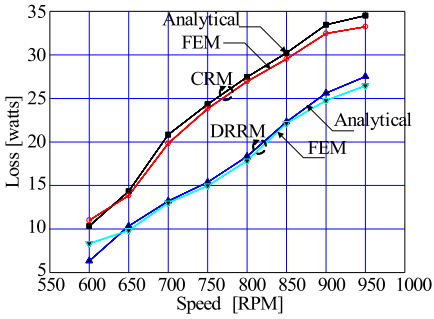

Figure 21. Loss characteristics.

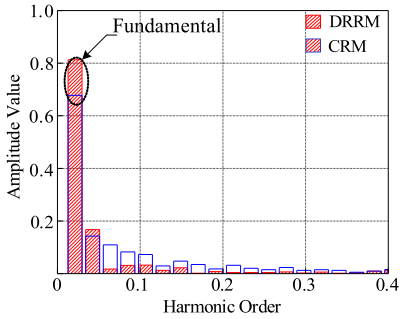

Figure 22. Comparison of harmonic components.

Table 5. Comparison evaluations using quality factor.

Machine	THD [%]	K_t [Nm]	K_m [Nm/A/W]	G [Nm/A/W/mm^3]
CRM	33.923	1.2692	0.0058	0.26868
DRRM	13.449	1.5559	0.0098	0.76648

6. CONCLUSIONS

The fundamental concepts in deriving the dual-air-gap structure is realised through the proposed novel structure, Double Rotor Reluctance Motor (DRRM). The numerical FEA tool is used for the analysis of such a structure to derive the electro-magnetic

characteristics. A comparative evaluation of the double rotor reluctance machine with that of the conventional reluctance machine is performed. The maximum torque generated by the selected dual-air-gap structure is 1.7549 Nm and for conventional structure is 1.2723 Nm. Also, the dual-air-gap structure exhibits 65% increase in average torque value compared with that of the conventional single-air-gap structure.

REFERENCES

1. Miller, T. J. E., *Switched Reluctance Motors and Their Control*, Magna Physics and Clarendon Press, Oxford, 1993.
2. Krishnan, R., *Design Procedure for Switched-reluctance Motors Design*, Wiley-Interscience, New York, 2001.
3. Aravind, C. V., M. Norhisam, I. Aris, M. H. Marhabhan, D. Ahmad, and M. Nirei, "Double rotor switched reluctance motors: Fundamentals and magnetic circuit analysis," *IEEE Student Conference on Research and Development (SCORED2011)*, 294–299, Cyberjaya, Malaysia, Dec. 19–20, 2011.
4. Norhisam, M., K. C. Wong, N. Mariun, and H. Wakiwaka, "Double side interior permanent magnet linear synchronous motor and drive system," *International Conference on Power Electronics and Drives Systems, PEDS*, Vol. 2, 1370–1373, Nov. 28-01, 2005.
5. Norhisam, M., S. Ridzuan, R. N. Firdaus, C. V. Aravind, H. Wakiwaka, and M. Nirei, "Comparative evaluation on power-speed density of portable permanent magnet generators for agricultural application," *Progress In Electromagnetic Research*, Vol. 129, 345–363, 2012.
6. Norhisam, M, M. Norafiza, and C. Y. Sia, "Double stator type permanent magnet generator," *2009 IEEE Student Conference on Research and Development (SCOReD)*, 316–319, Nov. 16–18, 2009.
7. Zhang, D., S. X. Niu, K. T. Chau, J. Z. Jiang, and Y. Gong, "Design and analysis of a double-stator cup-rotor directly driven permanent magnet wind power generator," *CES/IEEE 5th International Power Electronics and Motion Control Conference*, Vol. 3, 1–5, Aug. 14–16, 2006.
8. Peng, W., F. G. Zhang, and J.-W. Ahn, "Design and control of a novel bearingless SRM with double stator," *2012 IEEE International Symposium on Industrial Electronics (ISIE)*, 1928–1933, May 28–31, 2012.
9. Li, L. B., Q. Y. Zhao, G. K. Shi, and H. J. Wang, "Analysis of feasibility of double-rotor motor applied to hybrid electric

vehicle," *Vehicle Power and Propulsion Conference*, 1–5, Sep. 3–5, 2008.

10. Hoeijmakers, M. J. and J. A. Ferreira, "The electric variable transmission," *IEEE Transactions on Industry Applications*, Vol. 42, No. 4, 1092–1100, Jul.–Aug. 2006.
11. Liu, C. and K. T. Chau "Electromagnetic design and analysis of double rotor flux modulated permanent magnet machines," *Progress In Electromagnetics Research*, Vol. 131, 81–97, 2012.
12. Torkaman, H. and E. Afjei, "Radial force characteristic assessment in a novel two-phase dual layer SRG using FEM," *Progress In Electromagnetics Research*, Vol. 125, 185–202, 2012.
13. Cui, S. M., Y. J. Yuan, and T. C. Wang, "Research on switched reluctance double-rotor motor used for hybrid electric vehicle," *International Conference on Electrical Machines and Systems, ICEMS*, 3393–3396, Oct. 17–20, 2008.
14. Norhisam, M., C. V. Aravind, H. Marhaban, I. Aris, and M. Nirei, "Multi-rotor reluctance motor," Malaysian Intellectual Property Filing Agency, Malaysia, Mar. 2013.
15. Torkaman, H. and E. Afjei, "Comparison of three novel types of two-phase switched reluctance motors using finite element method," *Progress In Electromagnetics Research*, Vol. 125, 151–164, 2012.
16. Torkaman, H. and E. Afjei, "FEM analysis of angular misalignment fault in SRM magnetostatic characteristics," *Progress In Electromagnetics Research*, Vol. 104, 31–48, 2010.
17. Mahmoudi, A., N. A. Rahim, and H. W. Ping, "Axial-flux permanent-magnet motor design for electric vehicle direct drive using sizing equation and finite element analysis," *Progress In Electromagnetics Research*, Vol. 122, 467–496, 2012.
18. Kameari, A., "Local force calculation in 3D FEM with edge elements," *International Journal of Applied Electromagnetics in Materials*, Vol. 3, 231–240, 1993.
19. Aravind C. V., M. Norhisam, M. H. Marhaban, and I. Aris, "Analytical design of double rotor switched reluctance motor using optimal pole arc values," *International Review in Electrical and Electronics*, Vol. 7, No. 1, 3314–3324, Feb. 2012.
20. http://www.youtube.com/watch?v=orD2m7jV3MU.